Appl Phys A (2009) 96: 873–886
DOI 10.1007/s00339-009-5140-3

Applied Physics A
Materials Science & Processing

Effect of growth rate and Mg content on dendrite tip characteristics of Al–Cu–Mg ternary alloys

A. Berkdemir · M. Gündüz

Received: 6 August 2008 / Accepted: 4 February 2009 / Published online: 3 March 2009

Abstract An experimental analysis is presented to correlate the secondary dendrite arm spacing λ_2 and dendrite tip radius R with growth rate V and Mg content $C_{0\text{-Mg}}$ of Al–Cu–Mg ternary alloys. Under constant temperature gradient G (4.84 ± 0.13 K mm^{-1}), a series of directional solidification experiments were performed at five different growth rates V (16.7–83.3 μm/s) and five different Mg contents $C_{0\text{-Mg}}$ in Al–5 wt.% Cu–(0.5–5) wt.% Mg alloys. Solid–liquid interface was investigated from the longitudinal sections of the quenched samples, and λ_2 and R were measured on the dendrite tips. The dependencies of λ_2 and R on V and $C_{0\text{-Mg}}$ were determined. The experimental results showed that the values of λ_2 and R decrease as V and $C_{0\text{-Mg}}$ increase at a constant G. The present exponent values related to V are found to be slightly lower than the values of the theoretical models and previous experimental works; however, $C_{0\text{-Mg}}$ exponent values are found to be much lower than the theoretical models and previous experimental works. The ratio of the secondary dendrite arm spacing to the dendrite tip radius is 2.09 ± 0.15, in good agreement with the scaling law. At a constant $C_{0\text{-Mg}}$, the values of VR^2 were found to slightly increase with the ascending V. However, as $C_{0\text{-Mg}}$ increases, the values of VR^2 decrease.

PACS 68.70.+w · 64.70.D · 61.66.Dk · 81.30.Fb · 81.30.-t · 68.35.Rh

A. Berkdemir · M. Gündüz (✉)
Department of Physics, Faculty of Arts and Sciences, Erciyes University, 38039 Kayseri, Turkey
e-mail: gunduz@erciyes.edu.tr
Fax: +90-352-4374933

1 Introduction

How any substance—metal, plastic, water, or anything else—changes from a disordered liquid state to an ordered solid state determines many of its physical and mechanical properties and thus its usefulness in manufacture or construction. The microstructures formed during the solidification of materials are almost permanent and often very difficult to modify completely even during the post fabrication procedures [1]. Controlling solidification is a fundamental goal of material scientists and physicists. If we understand the process in detail, we can control it to accentuate desired properties. Solidification is important in an enormous number of industrial processes, since any metal or plastic product is usually melted and resolidified at some stage of its fabrication.

Dendritic structures evolve under two different growth conditions according to transport of latent heat of fusion away from the solid–liquid interface [2–4]. First, during the free growth (FG) from an undercooled melt, generally equiaxed dendrites form. In this case, the temperature gradient in the liquid at the solid–liquid interface is negative, whereas the one in the solid is nearly zero. Second, in directional solidification (DS) where a positive temperature gradient in the liquid is imposed, columnar dendrites develop. The dendrite growth direction and the heat flow direction are parallel for FG process, whereas they are antiparallel for DS process.

Directional solidification technique has been utilized to study the microstructure evolution and pattern formation since it provides an accurate and independent control of temperature gradient G, growth velocity V, and alloy composition C_0. During the directional solidification of alloys, the structure of the solid–liquid interface can be planar, cellular, or dendritic, depending on G, V and C_0. A majority of

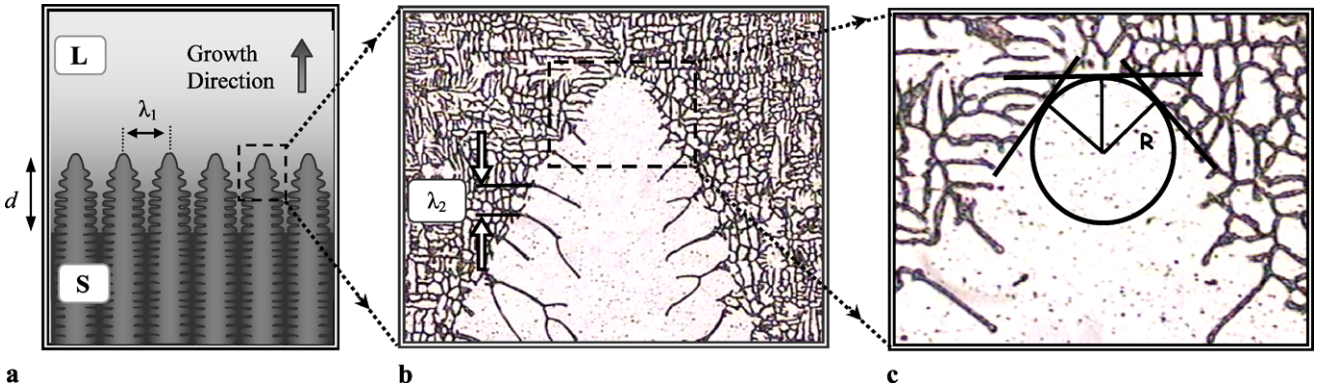

Fig. 1 (**a**) A schematic illustration of the dendritic morphology of the solid–liquid interface. Definitions of (**a**) primary dendrite arm spacing λ_1 and mushy zone depth d; (**b**) secondary dendrite arm spacing λ_2 and (**c**) dendrite tip radius R. (L: liquid, S: solid)

alloys grow under conditions which give rise to dendritic interfaces. The morphology of the dendritic solidification front ensures a high interface area-to-volume ratio that is more favorable for heat and mass redistribution compared to cellular and planar interface [5]. The formation of dendritic morphology has been explained by using heat and mass diffusion theories and including the effect of solid–liquid interface energy [6–11]. Recently, the anisotropy of the solid–liquid interface energy has been proven to be highly important for the morphology of the dendrite [12, 13].

Dendritic morphology is characterized with a single dendrite tip's microstructure parameters (secondary dendrite arm spacing λ_2 and dendrite tip radius R) and surrounding microstructure parameters (primary dendrite arm spacing λ_1 and mushy zone depth d) (Fig. 1). Most of the work devoted to obtain the dependency of dendritic microstructure parameters on solidification processing parameters (V, G, C_0) has been focused on the usage of binary metallic alloys or transparent organic alloys, and on obtaining the dependency of λ_1 on V and G [14–21]. However, the usage of ternary or multicomponent metallic alloys and, in particular, the observation of the effect of composition and growth rate on the secondary dendrite arm spacing and dendrite tip radius have been scarcely studied [22–27].

In this study, we consider the effect of V and $C_{0\text{-Mg}}$ on the single dendrite tip's microstructure parameters, namely on the secondary dendrite arm spacing λ_2 and dendrite tip radius R in the columnar dendritic growth as shown schematically in Fig. 1(a–c). The secondary dendrite arm spacing λ_2 determines the solute segregation profiles in a solidified material which can significantly influence the properties of the solidified alloys. The dendrite tip radius R is the most important length scale which governs various microstructural parameters of the dendritic structure. All other characteristic lengths of the dendritic structure are not only related to R, but also their evolution is controlled by R [28]. A literature survey shows several theoretical models [29–35] and experimental studies [22–27, 36–39] examining the influence of solidification processing parameters (G, V, C_0) on λ_2 and R. Results showed that λ_2 and R decrease with the increase of V and C_0.

Al–Cu–Mg alloys were among the first heat-treatable, high-strength Al alloys developed for structural applications and are widely used in automotive and aerospace because of their strength, ductility and superior creep strength at elevated temperatures [40–43]. Adding Mg to Al–Cu alloys increases strength without unduly decreasing the ductility. Alloy development and the control of the original solidification microstructure are important to achieve desired properties.

The aim of this work is to investigate the effect of V and $C_{0\text{-Mg}}$ on λ_2 and R in Al–Cu–Mg ternary alloys under well-controlled experimental conditions, and to compare the results with the current theoretical models [29–35] and previous experimental results [18, 44–62].

2 Background

2.1 The secondary dendrite arm spacing models

The initial secondary dendrite arm spacing λ_2, which develops immediately behind the primary dendrite tip, has a uniform spacing, whereas it increases with distance away from tip, or time because of the coarsening process [63, 64].

Langer and Müller-Krumbhaar [29] have carried out a detailed numerical analysis of the wavelength of instabilities along the sides of a dendrite and predicted scaling law

$$\lambda_2/R = 2.1 \pm 0.03. \tag{1}$$

Using this scaling law, the variation in λ_2 for small Peclet number conditions is given by Trivedi and Somboonsuk [30] as

$$\lambda_2 = (8\Gamma DL/kV\Delta T_0)^{1/2}, \tag{2}$$

where Γ is the Gibbs–Thomson coefficient, D is the solute diffusion coefficient in the liquid, k is partition coefficient, ΔT_0 is undercooling and $L = 1/2(l+1)(l+2)$ for the spherical approximation of dendrite where l is the harmonic of perturbation. Huang and Glicksman [62] found $l = 6$ to be operative for cubic materials. For both steady- and unsteady-state heat flow conditions, Bouchard and Kirkaldy [31] derived an expression relating λ_2 and tip growth rate V, independent of temperature gradient G and is given by

$$\lambda_2 = 2\pi a_2 \left(\frac{4\sigma}{C_0(1-k)^2 \Delta H} \left(\frac{D}{V} \right)^2 \right)^{1/3}, \tag{3}$$

where a_2 is the secondary dendrite calibrating factor, σ is solid–liquid surface energy, and ΔH is latent heat of fusion.

2.2 The dendrite tip radius models

Hunt [32], Kurz and Fisher [33], and Trivedi [34] have proposed the theoretical models to characterize dendrite tip radius R as a function of C_0 and V during steady-state growth conditions. According to Hunt Model [32]:

$$R = \left[2\Gamma D / m(k-1) \right]^{0.5} C_0^{-0.5} V^{-0.5}, \tag{4}$$

whereas the Kurz and Fisher Model [33] indicates that:

$$R = 2\pi \left[\Gamma D / m(k-1) \right]^{0.5} C_0^{-0.5} V^{-0.5}, \tag{5}$$

and according to Trivedi Model [34]:

$$R = \left[2\Gamma DL / m(k-1) \right]^{0.5} C_0^{-0.5} V^{-0.5}. \tag{6}$$

As can be seen from (4)–(6), the theoretical models for R are very similar and differ only by a constant. Langer and Müller-Krumbhaar [35] carried out a linear stability analysis of the tip region and obtained an expression for the marginally stable tip radius R

$$V R^2 = \Gamma D / \sigma^* k \Delta T_o, \tag{7}$$

where σ^* is stability constant which has a value of approximately 0.025. The above equation predicts that $V R^2$ is constant for a given composition. The composition dependence of (7) comes through ΔT_0 which is dictated by the phase diagram.

3 Experimental procedure

3.1 Sample preparation and solidification

Five different compositions of master alloys [Al–5 wt.%Cu–(0.5, 1, 2 3 5) wt.% Mg] were prepared by melting weighed quantities of (≥99.99 wt.%) Al, (≥99.99 wt.%) Cu and (≥99.99 wt.%) Mg in a graphite pot inserted in the vacuum melting furnace. After allowing time for melt homogenization, the molten master alloy was stirred and quickly poured into the holes drilled on the graphite rod, and then lowered to the cold region of the furnace. The molten master alloy was directionally frozen from bottom to top under vacuum. Afterwards, the sufficient amount of master alloy was placed in a funnel on top of the empty graphite crucible (200 mm in length, 4 mm ID and 6.35 mm OD) which was positioned in a Bridgman type furnace. The system was heated under argon atmosphere. Then the alloy was melted, stirred, and the crucible was filled with the alloy. After about 60 minutes to achieve the steady state thermal conditions in the furnace, the sample was withdrawn downward about 90–100 mm with a known pulling rate by means of a synchronous motor and then the sample rapidly quenched. The block diagram of the experimental set up is shown in Fig. 2. In order to see the $C_{0\text{-Mg}}$ and V effect on λ_2 an R, directional solidification experiments were repeated for five different alloy compositions [Al–5 wt.% Cu–(0.5, 1, 2 3 5) wt.% Mg] and five different growth rates (16.67–83.33 μm/s).

3.2 Measurement of temperature gradient G and growth rate V

The temperature of the Bridgman type furnace was controlled with a Eurotherm 905S type controller to an accuracy of ±0.1 K during the run. The experimental details are given in [65]. Three insulated K-type 0.25 mm diameter thermocouples with known distances were placed into a capillary alumina tube (0.8 mm ID, 1.2 mm OD) which was parallel to the heat flow direction inside the crucible. Temperature distribution in the sample was monitored via the output of three thermocouples positioned approximately 5 mm apart. All of the thermocouple leads were taken to an ice–water cold junction and to the data logger interfaced with a PC, and the temperatures were recorded simultaneously. When the third thermocouple was at the solid–liquid interface and the first and second thermocouples were in the liquid, their temperatures were used to obtain temperature gradient G.

It was found that the pulling speed was similar to the growth rate V; this may be due to the higher rate of atom attachment kinetics of metallic alloys and/or the graphite crucible which has good thermal conductivity. The growth rate was calculated with two different methods. In the first method, the values for the growth rate were calculated from the measurements of the time taken for the solid–liquid interface to pass the thermocouples separated by a known distance. In the second method, solidification time and the solidification distance (on the longitudinal section of the polished sample) were measured and the ratio of them gives the growth rate. The V values which are obtained from both methods were found to be similar with the pulling speed.

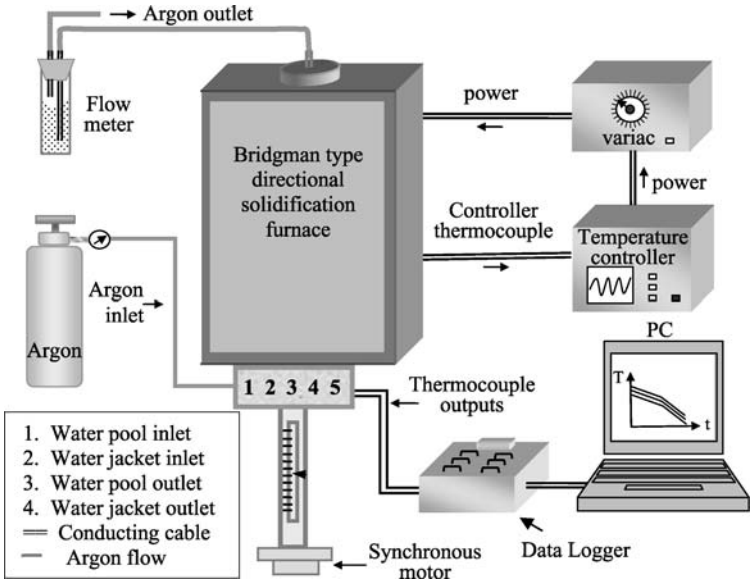

Fig. 2 Block diagram of the experimental set-up

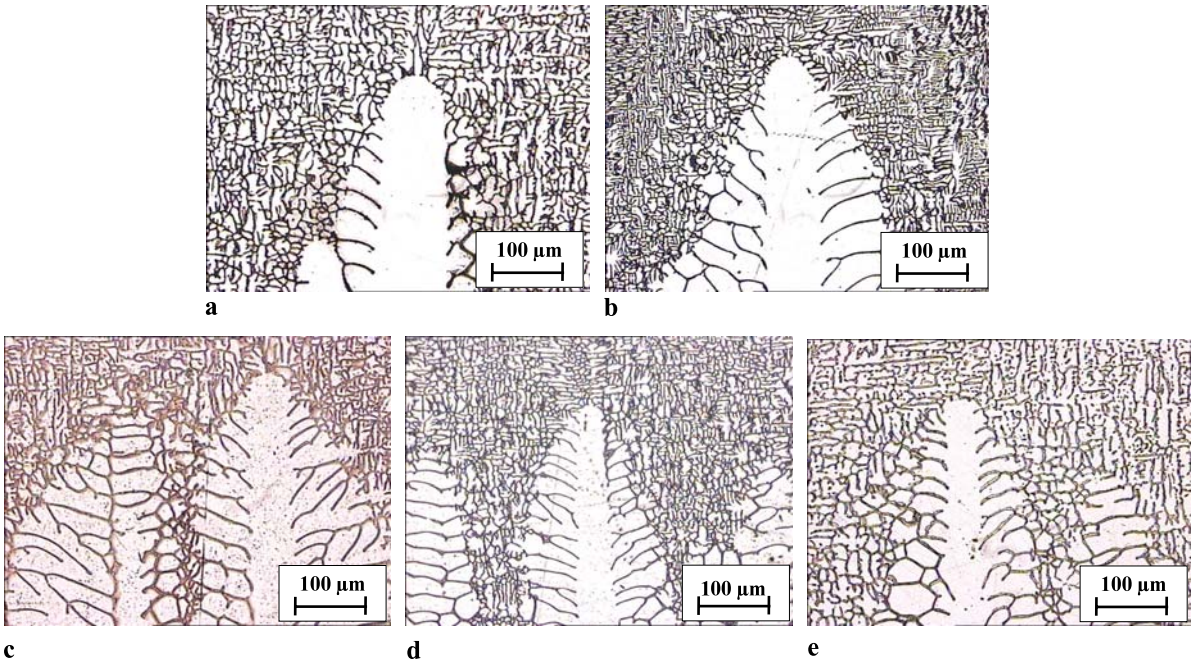

Fig. 3 Dendritic structures of directionally solidified Al–5 wt.% Cu–0.5 wt.% Mg alloys for different V at a constant $G = 4.84 \pm 0.13$ K mm^{-1}: (**a**) $V = 16.67$ µm/s; (**b**) $V = 26.67$ µm/s; (**c**) $V = 41.67$ µm/s; (**d**) $V = 66.67$ µm/s; (**e**) $V = 83.33$ µm/s

3.3 Metallographic examination

The directionally grown quenched specimen was removed from the graphite crucible, and then it was ground to observe the solid–liquid interface. The longitudinal section of the sample (10 mm) which included the quenched solid–liquid interface was separated from the sample and set in the mounting resin. The longitudinal sections of this part were ground, polished using diamond paste to a 1 µm finish and etched within the Keller's reagent to reveal the dendritic microstructure. The photographs of microstructures were taken with a CCD digital camera placed on the top of an Olympus BH-2 optical microscopy, (Figs. 3, 4).

3.4 Measurement of secondary dendrite arm spacing λ_2 and dendrite tip radius R

The secondary dendrite arm spacing λ_2 was measured from initial adjacent side branches of primary dendrite, see Fig. 1(b). Each of the side-branch spacing data reported here

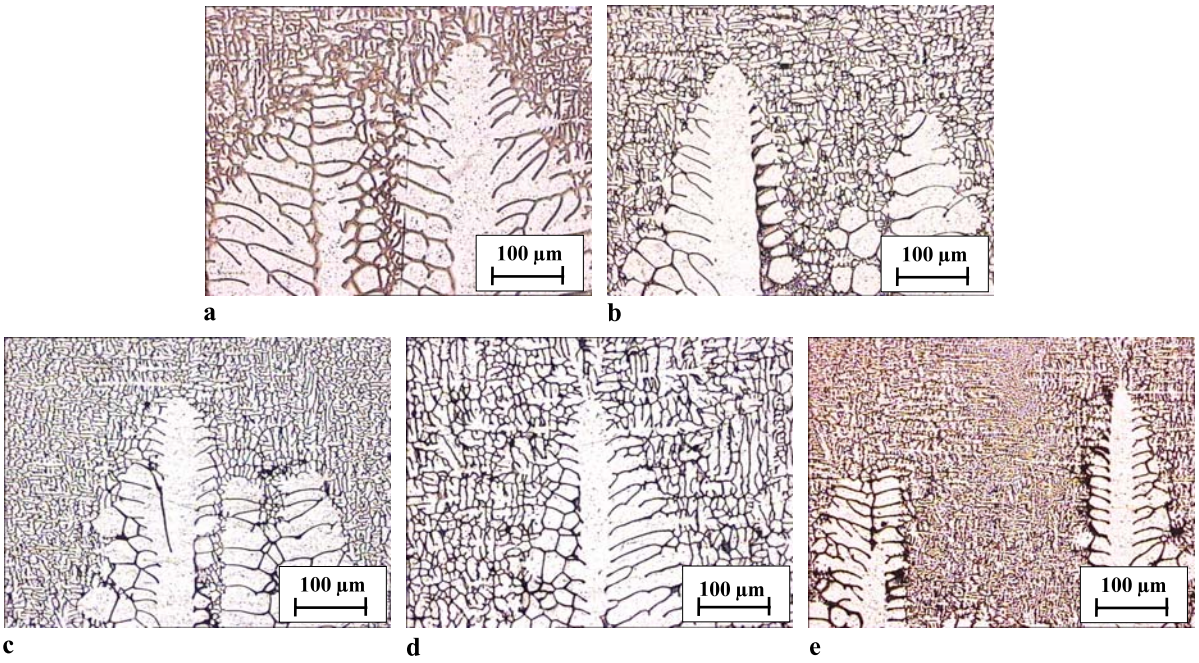

Fig. 4 Dendritic structures of directionally solidified Al–Cu–Mg alloys for different $C_{0\text{-Mg}}$ at a constant $V = 41.47$ µm/s and $G = 4.84 \pm 0.13$ K mm^{-1}. (**a**) Al–5 wt.% Cu–0.5 wt.% Mg; (**b**) Al–5 wt.% Cu–1 wt.% Mg; (**c**) Al–5 wt.% Cu–2 wt.% Mg; (**d**) Al–5 wt.% Cu–3 wt.% Mg; (**e**) Al–5 wt.% Cu–5 wt.% Mg

was averaged over the 25–50 λ_2 measurements, depending on the growth conditions. As shown in Fig. 1(c), the tip radius R was measured by fitting a suitable circle on the dendrite tip side. These R measurements were repeated at least 10 times on dendrites for each specimen. For metallic systems, it is difficult to measure R. To get exact shape of dendrite tip region, several grindings and polishings were made in the longitudinal section of the specimen. Photographs of each layer were taken from the same dendrite, and the best one which possesses the biggest R was chosen to be datum of R. The measured λ_2 and R values are given in Table 1. We tried to use parabola fitting method [66, 67], which is commonly used at transparent alloys, to measure R, but the results of the parabola fitting method were found to be rather scattered.

4 Results and discussion

4.1 Experimental results

A series of directional solidification experiments were carried out with five different compositions of [Al–5 wt.%Cu–(0.5, 1, 2 3 5) wt.% Mg] and five different growth rates (16.67–83.33 µm/s) at a constant $G = 4.84 \pm 0.13$ K mm^{-1}. Figures 3 and 4 show the typical longitudinal views of microstructures studied to examine the effect of V and $C_{0\text{-Mg}}$ on the λ_2 and R. The measured λ_2 and R values with standard deviations are given in Table 1. The variation of λ_2 and R with V and $C_{0\text{-Mg}}$ was plotted in Figs. 5 and 6. From each line on these graphs, linear regression analysis was carried out to find experimental power law expressions and proportionality constants. The results are given in Table 2 and the power law dependencies of λ_2 and R on V and $C_{0\text{-Mg}}$ were obtained from Figs. 5 and 6.

4.2 Effect of V on λ_2 and R

As can be seen from Tables 1, 2 and Figs. 3, 5, an increase in the growth rate, V, leads to a decrease in λ_2 and R for a given constant initial Mg content for directionally solidified Al–Cu–Mg ternary alloys. From Fig. 5, the dependencies of λ_2 and R on V are obtained by the linear regression analysis and yield the relations in the following form:

$$\lambda_2 = k_1 V^{-a}, \tag{8}$$

$$R = k_2 V^{-b}, \tag{9}$$

where k_1 and k_2 are proportionality constants, a and b are the growth rate exponent values of λ_2 and R, respectively. The values of exponents a and b were obtained as 0.32 and 0.41, respectively. The theoretical models predict the growth rate exponent values of λ_2 as 1/2 and 2/3 [30, 31] and the growth rate exponent values of R as 1/2 [32–35], respectively. Therefore, our experimental results of the growth rate exponent values of λ_2 and R were lower than the values of the theoretical models. As can be seen from Table 2(a, b)

Table 1 (a) Variation of λ_2 (μm), R (μm), λ_2/R, and VR^2 with V and $C_{0-\mathrm{Mg}}$ at a constant G. (b) Variation of mean and standard deviations of VR^2 with $C_{0\text{-Mg}}$

(a)

V (μm/s)	Alloys																			
	Al–5 wt.% Cu–0.5 wt.% Mg				Al–5 wt.% Cu–1 wt.% Mg				Al–5 wt.% Cu–2 wt.% Mg				Al–5 wt.% Cu–3 wt.% Mg				Al–5 wt.% Cu–5 wt.% Mg			
	λ_2	R	λ_2/R	VR^2 $\times 10^3$	λ_2	R	λ_2/R	VR^2 $\times 10^3$	λ_2	R	λ_2/R	VR^2 $\times 10^3$	λ_2	R	λ_2/R	VR^2 $\times 10^3$	λ_2	R	λ_2/R	VR^2 $\times 10^3$
16.67	39.12 ±1.54	20.91 ±0.77	1.87	7.29	33.13 ±2.17	17.80 ±0.45	1.86	5.28	27.92 ±1.65	14.81 ±0.80	1.89	3.66	25.61 ±1.58	12.87 ±0.64	1.99	2.76	23.84 ±1.68	11.34 ±0.48	2.10	2.14
26.67	33.87 ±2.43	17.40 ±0.36	1.95	8.07	27.84 ±1.51	14.96 ±0.49	1.86	5.97	24.23 ±1.54	12.25 ±0.57	1.98	4.00	22.29 ±1.47	10.93 ±0.41	2.02	3.19	20.10 ±1.51	9.26 ±0.55	2.17	2.29
41.67	29.90 ±2.06	14.68 ±0.54	2.04	8.98	24.23 ±1.62	12.14 ±0.46	2.00	6.14	21.56 ±2.37	10.37 ±0.36	2.08	4.48	19.33 ±1.38	8.95 ±0.56	2.16	3.34	17.70 ±2.32	7.82 ±0.45	2.26	2.55
66.67	25.26 ±1.12	11.98 ±0.61	2.11	9.58	21.52 ±0.88	10.41 ±0.39	2.07	7.22	18.56 ±1.54	8.78 ±0.41	2.11	5.14	16.75 ±0.84	7.58 ±0.34	2.18	3.83	15.34 ±1.53	6.44 ±0.37	2.38	2.77
83.33	23.37 ±0.85	10.65 ±0.34	2.19	9.46	19.29 ±1.37	9.17 ±0.34	2.10	7.01	16.37 ±1.12	7.44 ±0.46	2.20	4.61	15.21 ±1.09	6.53 ±0.25	2.33	3.55	14.03 ±0.96	5.82 ±0.30	2.41	2.83

(b)

Alloys	Al–5 wt.% Cu–0.5 wt.% Mg	Al–5 wt.% Cu–1 wt.% Mg	Al–5 wt.% Cu–2 wt.% Mg	Al–5 wt.% Cu–3 wt.% Mg	Al–5 wt.% Cu–5 wt.% Mg
$VR^2 \times 10^3$ ($\mu m^3/s$)	8.67 ± 0.97	6.32 ± 0.79	4.38 ± 0.57	3.37 ± 0.43	2.51 ± 0.30

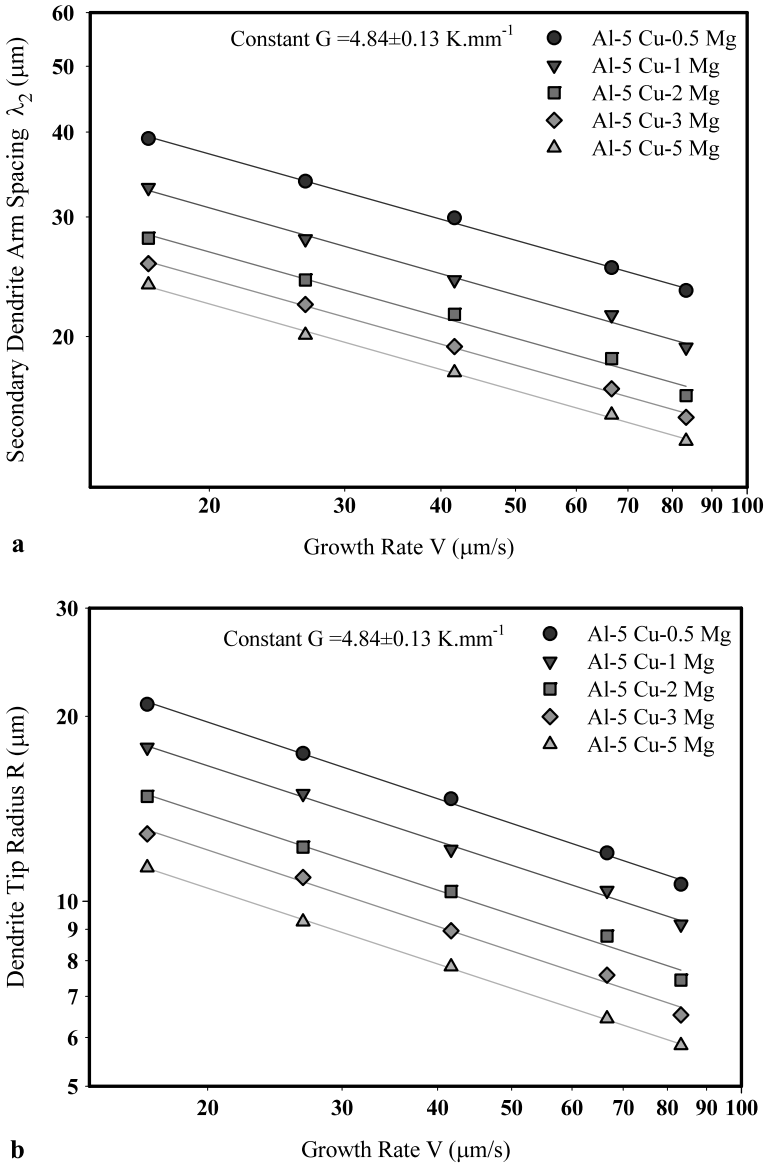

Fig. 5 (**a**) Variation of λ_2 with growth rate V for five different $C_{0\text{-Mg}}$ at a constant G. (**b**) Variation of R with growth rate V for five different $C_{0\text{-Mg}}$ at a constant G

growth rate exponents of λ_2 and R do not change with the increasing $C_{0\text{-Mg}}$, but proportionality constants decrease with the increasing $C_{0\text{-Mg}}$. So λ_2 and R decrease not only with the increasing V, but also with $C_{0\text{-Mg}}$ values. This might be due to the dependency of proportionality constants which include material properties such as Γ, D, k, m, ΔH, σ (see (2)–(6)).

4.3 Effect of $C_{0\text{-Mg}}$ on λ_2 and R

As can be seen from Tables 1, 2 and Figs. 4, 6, both λ_2 and R are found to decrease with the Mg content $C_{0\text{-Mg}}$. From Fig. 6, the dependencies of λ_2 and R on $C_{0\text{-Mg}}$ are obtained by the linear regression analysis and yield the relations in the following form:

$$\lambda_2 = k_3 C_{0-\text{Mg}}^{-m}, \tag{10}$$

$$R = k_4 C_{0-\text{Mg}}^{-n}, \tag{11}$$

where k_3 and k_4 are proportionality constants, m and n are the Mg content exponent values of λ_2 and R, respectively. The values of exponents m and n were found to be 0.22 and 0.27, respectively. The theoretical models predict the composition exponent values of λ_2 as 1/2 and 2/3 [30, 31] and the composition exponent values of R as 1/2 [32–35], respectively. Therefore, the experimental results of the exponent values related to the composition of λ_2 and R were lower than the values of the theoretical models. As can be seen from Table 2(c, d) the Mg content exponents of λ_2 and R do not change with the increasing V, but proportionality constants decrease with the increasing V. Here again, the change in the proportionality constants might be due to the dependency of proportionality constants, which include material properties such as Γ, D, k, m, ΔH, σ (see (2)–(6)).

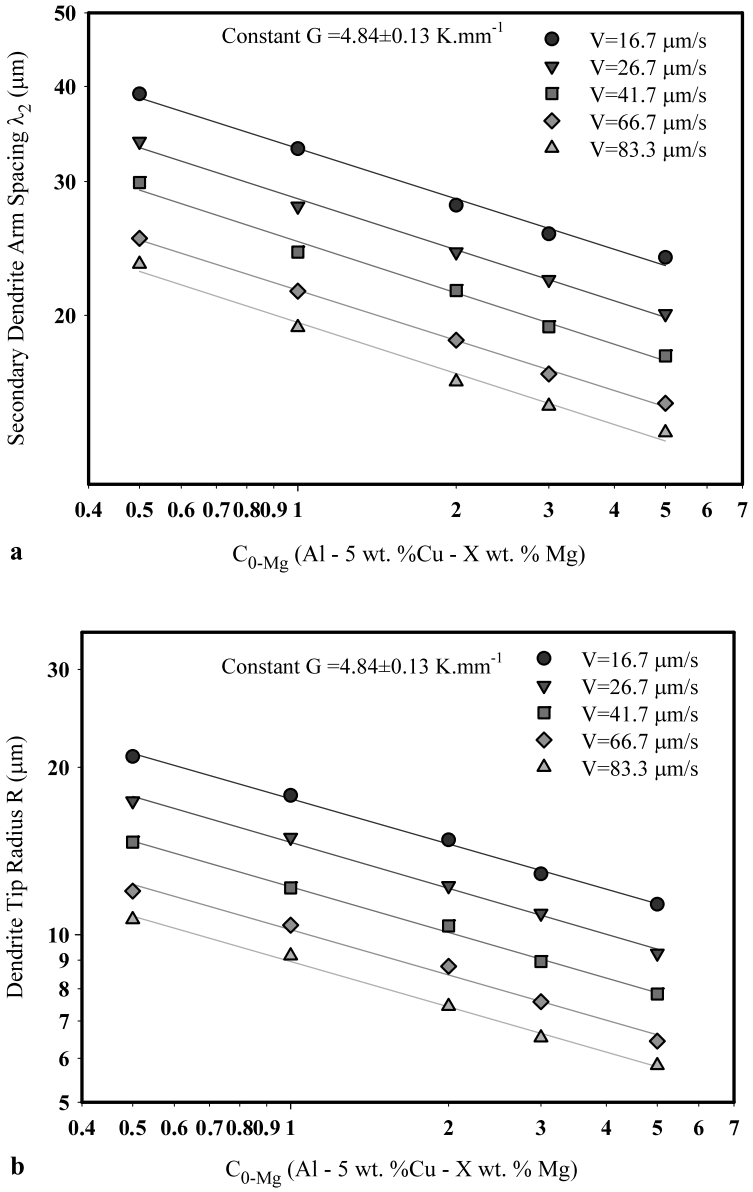

Fig. 6 (**a**) Variation of λ_2 with Mg content $C_{0\text{-Mg}}$ for five different V at a constant G. (**b**) Variation of R with Mg content $C_{0\text{-Mg}}$ for five different V at a constant G

4.4 Comparison of the experimental results with the models and previous works

Thermophysical data for Al-rich Al–Cu–Mg alloys used in the model calculations are given in Appendix A. Since the partition coefficient k and the melting range of the alloy ΔT_0 depend on alloy composition, k and ΔT_0 cannot be taken as constant at a wide range of Mg content of Al–5 wt.% Cu–(0.5, 1, 2 3 5) wt.% Mg alloy. Therefore, at each different $C_{0\text{-Mg}}$, relevant k and ΔT_0 used in the model calculations were found from 5 wt.% Cu vertical section of Al–Cu–Mg phase diagram (Appendices A, B) [68]. Most of the theoretical models for the prediction of solidification microstructures have been developed essentially for the limiting case of dilute alloys, leading the assumption of constant k. Several researchers [69, 70] investigated the influence of partition coefficient k on dendrite tip radius R, and found that the effect of the phase diagram on R is significant when k is not constant.

The experimental results of this work were compared with the results of the theoretical calculations from (2) and (3) for λ_2 and are shown in Fig. 7. The theoretical prediction of exponent values of solidification processing parameters (V and $C_{0\text{-Mg}}$) for λ_2 are given as $C_{0\text{-Mg}}^{-1/2}V^{-1/2}$ in Trivedi and Somboonsuk Model [30] and $C_{0\text{-Mg}}^{-1/3}V^{-2/3}$ in Bouchard–Kirkaldy Model [31]. In Fig. 7(a, b), it is seen that the collapse of experimental data on a single curve is achieved for two different abscissas. Hence, λ_2 was plotted as functions of the solidification processing parameters' dependencies, and it was found that the experimental exponent values of λ_2 have weaker dependencies on solidifica-

Table 2 Dependency of λ_2 and R on V and C_{0-Mg} at a constant G

$C_{0\text{-Mg}}$	(a) Dependency of λ_2 on V ($\lambda_2 = kV^{-a}$)			(b) Dependency of R on V ($R = kV^{-b}$)		
(Al–5 Cu–X Mg) wt.%	Relationships	Constant (k) ($\mu m^{1.32}$ $s^{-0.32}$)	Correlation coefficients (r)	Relationships	Constant (k) ($\mu m^{1.41}$ $s^{-0.41}$)	Correlation coefficients (r)
0.5	$\lambda_2 = k_1 V^{-0.32}$	$k_1 = 96.66$	$r_1 = -0.999$	$R = k_6 V^{-0.41}$	$k_6 = 67.70$	$r_6 = -0.999$
1	$\lambda_2 = k_2 V^{-0.32}$	$k_2 = 81.26$	$r_2 = -0.997$	$R = k_7 V^{-0.41}$	$k_7 = 56.19$	$r_7 = -0.998$
2	$\lambda_2 = k_3 V^{-0.32}$	$k_3 = 69.24$	$r_3 = -0.994$	$R = k_8 V^{-0.41}$	$k_8 = 47.13$	$r_8 = -0.995$
3	$\lambda_2 = k_4 V^{-0.32}$	$k_4 = 63.32$	$r_4 = -0.999$	$R = k_9 V^{-0.41}$	$k_9 = 41.78$	$r_9 = -0.997$
5	$\lambda_2 = k_5 V^{-0.32}$	$k_5 = 58.43$	$r_5 = -0.999$	$R = k_{10} V^{-0.41}$	$k_{10} = 35.81$	$r_{10} = -1.000$
V (μm/s)	(c) Dependency of λ_2 on $C_{0\text{-Mg}}$ ($\lambda_2 = kC_{0\text{-Mg}}^{-m}$)			(d) Dependency of R on $C_{0\text{-Mg}}$ ($R = kC_{0\text{-Mg}}^{-n}$)		
	Relationships	Constant (k) [μm (wt.%)$^{0.22}$]	Correlation coefficients (r)	Relationships	Constant (k) [μm (wt.%)$^{0.27}$]	Correlation coefficients (r)
16.67	$\lambda_2 = k_{11} C_{0\text{-Mg}}^{-0.22}$	$k_{11} = 33.17$	$r_{11} = -0.996$	$R = k_{16} C_{0\text{-Mg}}^{-0.27}$	$k_{16} = 17.57$	$r_{16} = -0.998$
26.67	$\lambda_2 = k_{12} C_{0\text{-Mg}}^{-0.22}$	$k_{12} = 28.48$	$r_{12} = -0.997$	$R = k_{17} C_{0\text{-Mg}}^{-0.27}$	$k_{17} = 14.67$	$r_{17} = -0.997$
41.67	$\lambda_2 = k_{13} C_{0\text{-Mg}}^{-0.22}$	$k_{13} = 25.02$	$r_{13} = -0.994$	$R = k_{18} C_{0\text{-Mg}}^{-0.27}$	$k_{18} = 12.20$	$r_{18} = -0.998$
66.67	$\lambda_2 = k_{14} C_{0\text{-Mg}}^{-0.22}$	$k_{14} = 21.59$	$r_{14} = -0.999$	$R = k_{19} C_{0\text{-Mg}}^{-0.27}$	$k_{19} = 10.21$	$r_{19} = -0.994$
83.33	$\lambda_2 = k_{15} C_{0\text{-Mg}}^{-0.22}$	$k_{15} = 19.58$	$r_{15} = -0.994$	$R = k_{20} C_{0\text{-Mg}}^{-0.27}$	$k_{20} = 8.95$	$r_{20} = -0.998$

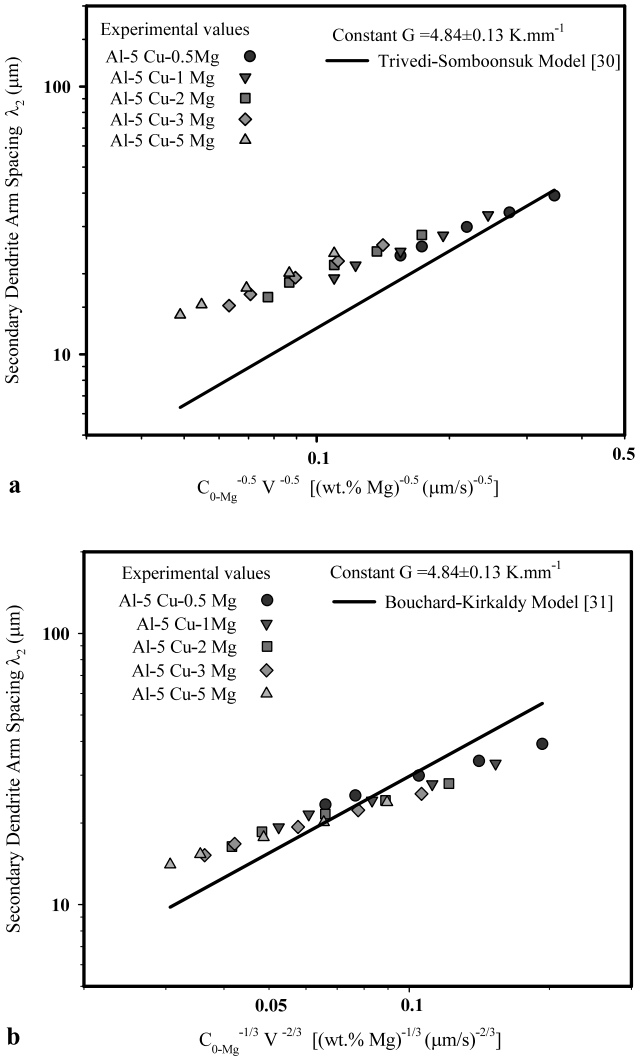

Fig. 7 (**a**) Comparison of the experimental and prediction of Trivedi–Somboonsuk Model [30] of λ_2 values as a function of $C_{0-Mg}^{-1/2} V^{-1/2}$. (**b**) Comparison of the experimental and prediction of Bouchard–Kirkaldy Model [31] of λ_2 values as a function of $C_{0\text{-Mg}}^{-1/3} V^{-2/3}$

tion processing parameters as expected in both models. As the slope of the line formed by the experimental points is obviously different from the slope of the theoretical models, it can be concluded that both theoretical models are invalid for predicting the size of the secondary arms for the metallic alloy systems. So, metallic alloy systems need more accurate theoretical models for forecasting the value of secondary dendrite arm spacing. Our experimental results agree quite well with the Trivedi–Somboonsuk Model's results for the higher values of $C_{0\text{-Mg}}^{-1/2} V^{-1/2}$, whereas discrepancies increase for smaller values of $C_{0\text{-Mg}}^{-1/2} V^{-1/2}$ value (Fig. 7(a)). Bouchard–Kirkaldy Model's results agree well with the experimental results for $C_{0\text{-Mg}}^{-1/3} V^{-2/3}$ values between 0.06–

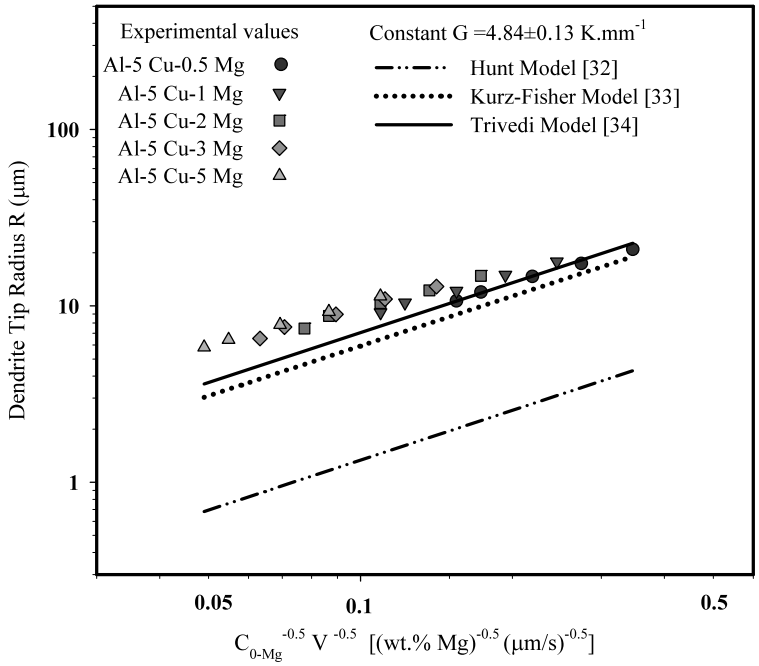

Fig. 8 Comparison of the existing theories of R with the experimental data in the Al–Cu–Mg system at a constant G

0.15. Outside of these values, discrepancies are increased (Fig. 7(b)).

Predictions of dendrite tip radius R by Hunt [32], Kurz–Fisher [33] and Trivedi [34] Models are shown in Fig. 8 with relevant experimental data. As can be seen from (4)–(6), the theoretical models for R are very similar and differ only by a constant. From Fig. 8, our experimental results for R are slightly higher than the predictions of Trivedi and Kurz–Fisher Models; however, the R value from the Hunt Model is several orders of magnitude lower than our results. It was seen that, as the Mg content of the alloy increases, the discrepancy between the experimental values and the theoretical predictions of R is increased. This might be due to the theoretical models which were developed for dilute alloy systems.

A number of experimental studies have been reported in the literature to characterize the variation in the λ_2 and R as functions of V and C_0, and it is given in Table 3. If one compares the present exponent values of λ_2 and R with the previous works, one can see that our experimental growth rate exponent values of λ_2 are slightly lower than some of previously reported ones [44, 48–51] and similar to some of previous results [45–48]; the present exponent values of R are slightly lower than the most of the previous results [48, 49, 51, 53, 55, 58–61] and are similar to some of them [50, 56, 57]. However, composition exponent values of λ_2 and R were found to be much lower than the other experimental results [52–54, 57, 61].

The variation of the λ_2/R values with V for Al–5 wt.% Cu–(0.5, 1, 2 3 5) wt.% Mg alloys for constant G are given in Table 1 and Fig. 9. In this study, the average value of

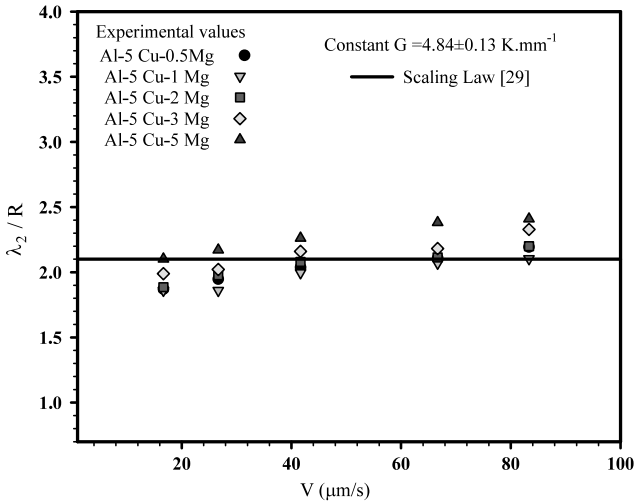

Fig. 9 Variation of λ_2/R with V for five different magnesium content $C_{0\text{-Mg}}$ at a constant G

λ_2/R is found to be 2.09 ± 0.15, which is in excellent agreement with the theoretical prediction of $\lambda_2/R = 2.1 \pm 0.3$ for undercooled dendrites [29]. A comparison of the values of λ_2/R obtained in the present work and the previous experimental works [18, 48–53, 55, 58, 60, 62] is also given in Table 4. It can be seen that the scaling constant increases with the degree of anisotropy of the system. Consequently, such a scaling law between λ_2 and R would seem to be a fundamental characteristic of the dendritic structure, although the value of the constant appears to depend slightly upon the initial composition C_0, anisotropy of the system,

Table 3 Some experimental results for λ_2 and R related to V and C_0 in the literature

Alloy	G (K mm^{-1})	V (μm s^{-1})	Relationships	Ref.
Al–[5 Cu–(0.5–5) Mg] wt.%	4.84	16.67–83.33	$\lambda_2 = kV^{-0.32}$	This work
Fe–(1.48 C–1.14 Mn) wt.%	5.3	8–210	$\lambda_2 = kV^{-0.45}$	[44]
Zn–(1.54–2.79) wt.% Mg	15–95	10–21800	$\lambda_2 = kV^{-0.33}$	[45]
Zn–(0.54–3.06) wt.% Mg	15	1–8000	$\lambda_2 = kV^{-0.33}$	[46]
Al–(5.7–20) wt.% Cu	90	8–360	$\lambda_2 = kV^{-0.29}$	[47]
Al–(3–24) wt.% Cu	6.3	8–490	$\lambda_2 = kV^{-(0.27-0.46)}$	[48]
SCN–5.5 mol% ACE[a]	6.7	0.4–100	$\lambda_2 = kV^{-0.56}$	[49]
SCN–(5–40) wt.% CTB	7.5	6.5–103.5	$\lambda_2 = kV^{-0.46}$	[50]
PVA–0.91 wt.% ETH	1.5	0.3–80	$\lambda_2 = kV^{-0.58}$	[51]
Al–[5 Cu–(0.5–5) Mg] wt.%	4.84	16.67–83.33	$\lambda_2 = kC_0^{-0.22}$	This work
Cd–(20–60) wt.% Pb	4.3	8.3–16.7	$\lambda_2 = kC_0^{-0.36}$	[52]
SCN–(5–40) wt.% CTB	7.5	6.5–103.5	$\lambda_2 = kC_0^{-0.36}$	[53]
SCN–(0.55–4) wt.% ACE	6.7	5.8	$\lambda_2 = kC_0^{-0.43}$	[54]
Al–[5 Cu–(0.5–5) Mg] wt.%	4.84	16.67–83.33	$R = kV^{-0.41}$	This work
Al–4.1 wt.% Cu	4	0.2–70	$R = kV^{-0.54}$	[53]
Al–(3–24) wt.% Cu	6.3	8–490	$R = kV^{-(0.39-0.60)}$	[48]
$NiAl_3$	5.4	2.7–32.0	$R = kV^{-0.62}$	[55]
SCN–(5–40) wt.% CTB	7.5	6.5–103.5	$R = kV^{-0.45}$	[50]
SCN–5.5 mol% ACE[a]	6.7	0.4–100	$R = kV^{-0.53}$	[49]
SCN–2wt.% Salol	2.5	–	$R = kV^{-0.37}$	[56]
SCN–(5–20) wt.% Salol	4.5	6.7–112.4	$R = kV^{-(0.42-0.49)}$	[57]
SCN–1.3 wt.% ACE[a]	1.6–9.7	1.6–250	$R = kV^{-0.53}$	[58]
SCN–2 wt.% water	2.4–3.3	0.76–105	$R = kV^{-0.53}$	[59]
CBr_4–10.5 wt. C_2Cl_6	3	0.1–100	$R = kV^{-0.53}$	[60]
CBr_4–7.9 wt. C_2Cl_6	3	0.1–100	$R = kV^{-0.47}$	[60]
PVA–0.91 wt.% ETH	1.5	0.3–80	$R = kV^{-0.54}$	[51]
Al–[5 Cu–(0.5–5) Mg] wt.%	4.84	16.67–83.33	$R = kC_0^{-0.27}$	This work
Cd–(20–60) wt.% Pb	4.3	8.3–16.7	$R = kC_0^{-0.49}$	[52]
SCN–(0.55–4) wt.% ACE	6.7	5.8	$R = kC_0^{-0.48}$	[54]
SCN–(5–40) wt.% CTB	7.5	6.5–103.5	$R = kC_0^{-0.34}$	[53]
SCN–(5–20) wt.% Salol	4.5	6.7–112.4	$R = kC_0^{-(0.39-0.59)}$	[57]
Al–(2–20) wt.% Cu	7.5–16	6–33	$R = k(CV)^{-0.50}$	[61]

[a]SCN: succinonitrile; ETH: ethanol; ACE: acetone, PVA: pivalic acid, CTB: carbon tetrabromide

and the experimental conditions which affect the dendritic structures.

According to the theoretical model [35], the value of VR^2 is expected to be constant for a given composition. If we look at the VR^2 values in Table 1, for solidification velocities in the range of 16.67 to 83.33 μm/s, the values of VR^2 slightly increase with the ascending V value for a given composition; however, as $C_{0\text{-Mg}}$ increases the values of VR^2 decrease since in (4)–(7) the undercooling, ΔT_0, depends on composition. The mean value and standard deviations of VR^2 for the corresponding compositions of Al–Cu–Mg alloy are given in Table 1(b). From Fig. 10, the dependence of VR^2 on $C_{0\text{-Mg}}$ can be expressed by an expression of $VR^2 = k_5 C_{0\text{-Mg}}^{-0.54}$, where k_5 is a proportionality constant.

5 Conclusions

Directional solidification experiments have been carried out with Al–5 wt.%Cu–(0.5, 1, 2 3 5) wt.% Mg alloys in order to see the effect of growth rate V and Mg content $C_{0\text{-Mg}}$ on secondary dendrite arm spacing λ_2 and dendrite tip radius R. Solid–liquid interfaces were investigated from the longitudinal sections of the quenched specimens and λ_2 and R were measured on the dendrite tips.

Our experimental observations showed that the values of λ_2 and R decrease as V and $C_{0\text{-Mg}}$ increase for five different V (16.7–83.3 μm/s) and five different $C_{0\text{-Mg}}$ (0.5–5wt.% Mg) for a constant $G = 4.84 \pm 0.13$ K mm^{-1}.

The mathematical relationships for λ_2 and R related to V and $C_{0\text{-Mg}}$ have been obtained to be $\lambda_2 = k_i V^{-0.32}$, $R =$

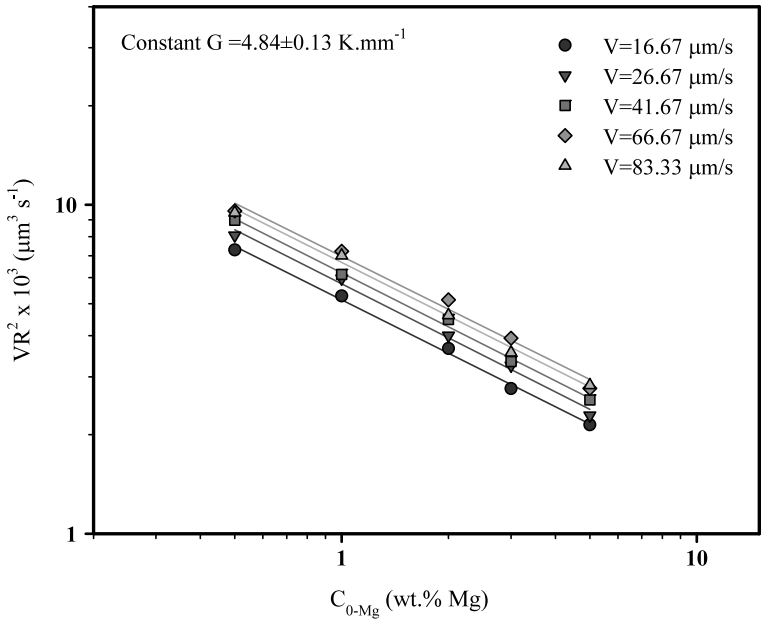

Fig. 10 Variation of VR^2 with $C_{0\text{-Mg}}$ for five different V at a constant G

Table 4 A comparison of λ_2/R values obtained in the present work with the theoretical and previous experimental works

System	λ_2/R values	Ref.
(theoretical value)	2.1 ± 0.03	[29]
Al–5 wt.%Cu–(0.5–5)wt.% Mg	2.09 ± 0.15	This work
Cd–(20–60) wt.% Pb	2.27 ± 0.14	[52]
Al–(3–24) wt.% Cu	2.8 ± 0.4	[48]
Al–4.1 wt.% Cu	2.7	[53]
Ni_3Al	3.0	[55]
SCN–1.3 wt.% ACE[a]	2.09 ± 0.15	[58]
SCN–(5–40) wt.% CTB	2.08	[50]
$CBr_4 - -10.5$ wt. C_2Cl_6	3.18	[60]
$CBr_4 - -7.9$ wt. C_2Cl_6	3.47	[60]
PVA–0.91 wt.% ETH	3.8	[51]
SCN–5.5 mol % ACE	2.2 ± 0.03	[49]
SCN	3.0	[62]
SCN	2.5	[18]
NH_4Cl–70 wt.% H_2O	3.7	[18]
SCN–5.6 wt.% H_2O	3.0	[18]

[a]SCN: succinonitrile; ETH: ethanol; ACE: acetone, PVA: pivalic acid, CTB: carbon tetrabromide

$k_j V^{-0.41}$, $\lambda_2 = k_k C_{0\text{-Mg}}^{-0.22}$, and $R = k_l C_0^{-0.27}$. The V and $C_{0\text{-Mg}}$ exponents of λ_2 and R were found to be constant, but proportionality constants of λ_2 and R (k_i, k_j, k_k, k_l) were found to be decreasing with both increasing V and $C_{0\text{-Mg}}$ values.

The present exponent values related to V were found to be slightly lower than the values of the theoretical models and previous experimental works; however, $C_{0\text{-Mg}}$ exponent values were found to be much lower than in the theoretical models and previous experimental works.

The ratio of the secondary dendrite arm spacing to the dendrite tip radius was 2.09 ± 0.15, in good agreement with the scaling law [29].

At a constant $C_{0\text{-Mg}}$, the values of VR^2 were found to slightly increase with the ascending V. However, as $C_{0\text{-Mg}}$ increases the values of VR^2 decrease.

Acknowledgements This work is supported by the Scientific Research Projects Council of Erciyes University under grant Nos. FBT-05-04 and FBA-05-22.

Appendix A

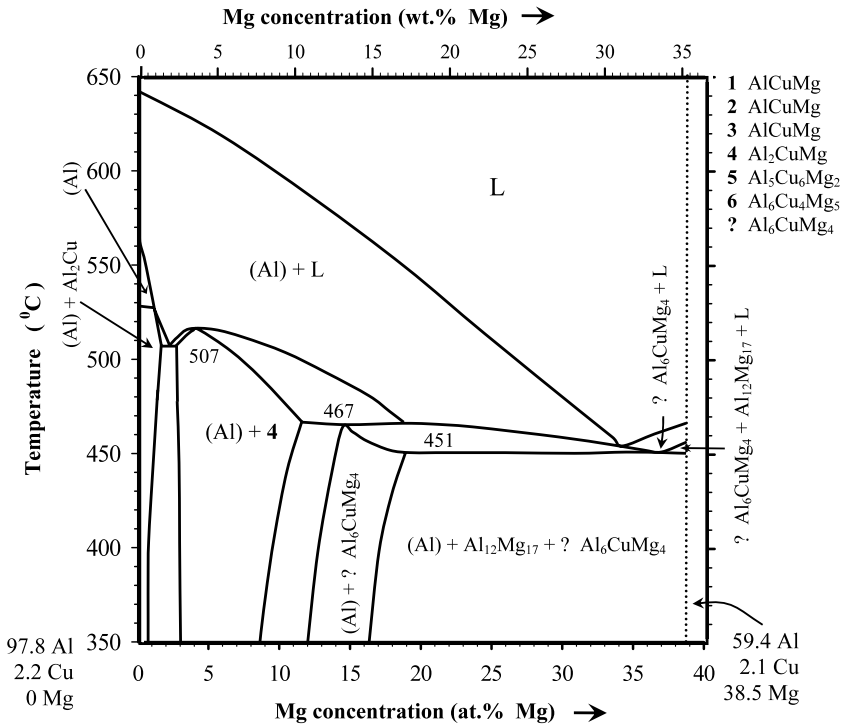

Fig. 11 5 wt.% Cu vertical section in Al-rich corner of Al–Cu–Mg ternary phase diagram [68]

Appendix B

Table 5 Thermophysical data for Al-rich Al–Cu–Mg alloys used in the model calculations

Property	Unit	*Value*	Ref.
Liquidus slope (m)	K (wt.% Mg)$^{-1}$	−5.07	[68]
Freezing range (ΔT_0) of			
Al–5 wt.% Cu–0.5 wt.% Mg alloy	K	89.70	[68]
Al–5 wt.% Cu–1 wt.% Mg alloy	K	111.77	[68]
Al–5 wt.% Cu–2 wt.% Mg alloy	K	127.22	[68]
Al–5 wt.% Cu–3 wt.% Mg alloy	K	112.37	[68]
Al–5 wt.% Cu–5 wt.% Mg alloy	K	104.95	[68]
Equilibrium partition coefficient (k) of			
Al–5 wt.% Cu–0.5 wt.% Mg alloy	–	0.03	[68]
Al–5 wt.% Cu–1 wt.% Mg alloy	–	0.06	[68]
Al–5 wt.% Cu–2 wt.% Mg alloy	–	0.10	[68]
Al–5 wt.% Cu–3 wt.% Mg alloy	–	0.14	[68]
Al–5 wt.% Cu–5 wt.% Mg alloy	–	0.23	[68]
Harmonic perturbations (L)	–	28	[49]
Secondary dendrite calibrating factor (a_2)	–	2.5	–
Solid-liquid surface energy (σ)[a]	J m^2	1.49×10^{-1}	[71]
Gibbs-Thomson coefficient (Γ)[a]	K m	1.30×10^{-5}	[71]
Liquid diffusion coefficient of Mg (D_L^{Mg})	m^2 s^{-1}	3×10^{-9}	[72]
Latent heat of fusion (ΔH)	J m^{-3}	9.5×10^8	[73]

[a]For Al–Mg alloy

References

1. J.A. Warren, IEEE Comput. Sci. Eng. **2**(2), 38 (1995)
2. W. Kurz, D. Fisher, *Fundamentals of Solidification* (Trans Tech., Aedermannsdorf, 1989)
3. Q. Li, C. Beckermann, J. Cryst. Growth **236**, 482 (2002)
4. S. Önel, T. Ando, Metall. Mater. Trans. A **39**, 2449 (2008)
5. D. Herlach *Interface and Transport Dynamics*, ed. by H. Emmerich, B. Nestler, M. Schreckenberg (Springer, Berlin, 2003), p. 26
6. G.P. Ivantsov, Dokl. Akad. Nauk SSSR **58**, 567 (1947)
7. J.S. Langer, H. Müller-Krumbhaar, Acta Metall. **26**, 1681 (1978)
8. J.A. Warren, J.S. Langer, Phys. Rev. A **42**, 3518 (1990)
9. J.J. Xu, Phys. Rev. A **43**, 930 (1990)
10. M. Ben Amar, E. Brener, Phys. Rev. Lett. **71**, 589 (1993)
11. J.C. Ramirez, C. Beckermann, A. Karma, H.J. Diepers, Phys. Rev. E **69**, 051607 (2004)
12. F. Gonzales, M. Rappaz, Metall. Mater. Trans. A **37**, 2797 (2006)
13. J. Deschamps, M. Georgelin, A. Pocheau, Europhys. Lett. **76**, 291 (2006)
14. S.H. Han, R. Trivedi, Acta Metall. Mater. **42**, 25 (1994)
15. S.A. Moir, H. Jones, Mater. Lett. **12**, 142 (1991)
16. J.T. Mason, J.D. Verhoeven, R. Trivedi, Metall. Trans. A **15**, 1665 (1984)
17. C.M. Klaren, J.D. Verhoeven, R. Trivedi, Metall. Trans. A **11**, 1853 (1980)
18. S. Liu, S.Z. Lu, A. Hellawell, J. Cryst. Growth **234**, 751 (2002)
19. W. Wang, P.D. Lee, M. McLean, Acta Mater. **51**, 2971 (2003)
20. D. Ma, Metall. Mater. Trans. B **33**, 223 (2002)
21. L. Li, A. Overfelt, J. Mater. Sci. **37**, 3221 (2002)
22. D.G. McCartney, J.D. Hunt, Acta Metall. **29**, 1851 (1981)
23. J.A. Horwath, L.F. Mondolfo, Acta Metall. **10**, 1037 (1962)
24. M.A. Chopra, M.E. Glicksman, N.B. Singh, Metall. Trans. A **19**, 3087 (1988)
25. T. Okamoto, K. Kishitake, J. Cryst. Growth **29**, 137 (1975)
26. H. Tian, D.M. Stefanescu, Metall. Trans. A **23**, 681 (1992)
27. B. Zlaticanin, S. Duric, B. Jordovic, B. Radonjic, Mater. Sci. Tech. **20**, 138 (2004)
28. R. Trivedi, W. Kurz, Int. Mater. Rev. **39**, 49 (1994)
29. H. Müller-Krumbhaar, J.S. Langer, Acta Metall. **29**, 145 (1980)
30. R. Trivedi, K. Somboonsuk, Mater. Sci. Eng. **65**, 65 (1984)
31. D. Bouchard, J. Kirkaldy, Metall. Mater. Trans. B **28**, 651 (1997)
32. J.D. Hunt, *Solidification and Casting of Metals* (The Metals Society, London, 1979), Book 192, p. 3
33. W. Kurz, D.J. Fisher, Acta Metall. **29**, 11 (1981)
34. R. Trivedi, Metall. Trans. A **15**, 977 (1984)
35. J.S. Langer, H. Müller-Krumbhaar, Acta Metall. **26**, 1681 (1978)
36. S.N. Tewari, Metall. Trans. A **17**, 2279 (1986)
37. L. Yu, G.L. Ding, J. Reye, S.N. Ojha, S.N. Tewari, Metall. Mater. Trans. A **30**, 2463 (1999)
38. M. Vijayakumar, S. Tewari, J.E. Lee, P.A. Curreri, Mater. Sci. Eng. A **132**, 195 (1991)
39. S. Liu, J. Li, J. Lee, R. Trivedi, Philos. Mag. **86**, 3717 (2006)
40. I.J. Polmear, *Light Alloys: Metallurgy of the Light Metals* (Willey, New York, 1995)
41. D.P. Bishop, J.R. Cahoon, M.C. Chaturvedi, G.J. Kipouros, W.F. Caley, Mat. Sci. Eng. A **290**, 16 (2000)
42. P.P. Date, K.A. Padmanabhan, J. Mater. Process. Technol. **112**, 68 (2001)
43. M. Song, Y. He, D. Xiao, B. Huang, Mater. Des. **30**, 857 (2009)
44. H. Jacobi, K. Schwerdtfeger, Metall. Trans. A **7**, 811 (1976)
45. H.Y. Liu, H. Jones, J. Mater. Sci. Lett. **11**, 769 (1992)
46. H.Y. Liu, H. Jones, Acta Metall. **40**, 229 (1992)
47. M.A. Taha, Metal Sci. **13**, 9 (1979)
48. M. Gündüz, E. Çadırlı, Mater. Sci. Eng. A **327**, 167 (2002)
49. K. Somboonsuk, J.T. Mason, R. Trivedi, Metall. Trans. A **15**, 967 (1984)
50. H. Kaya, E. Çadırlı, K. Keşlioğlu, N. Maraşlı, J. Cryst. Growth **276**, 583 (2005)
51. R. Trivedi, J.T. Mason, Metall. Trans. A **22**, 235 (1991)
52. A. Berkdemir, M. Gündüz, in *Solidification Processing*, ed. by H. Jones (University of Sheffield, Sheffield, 2007), p. 22
53. Y. Miyata, T. Suzuki, J.I. Uno, Metall. Trans. A **16**, 1799 (1985)
54. K. Somboonsuk, Ph.D. Thesis, Iowa State University, Ames, 1984, p. 53
55. H.K. Kim, J.C. Earthman, E.J. Lavernia, Mater. Sci. Eng. A **152**, 240 (1992)
56. M.J. Suk, Y.M. Park, Y.D. Kim, Scr. Mater. **57**, 985 (2007)
57. E. Çadırlı, İ. Karaca, H. Kaya, N. Maraşlı. J. Cryst. Growth **255**, 190 (2003)
58. H. Eseka, W. Kurz, J. Cryst. Growth **71**, 578 (1985)
59. C.A. Cattaneo, O.P. Evequoz, H.R. Bertorello, Scr. Metall. **31**, 461 (1994)
60. V. Seetharaman, L.M. Fabrietti, R. Trivedi, Metall. Trans. A **20**, 2567 (1989)
61. R.M. Sharp, A. Hellawell, J. Cryst. Growth **6**, 253 (1970)
62. S.C. Huang, M.E. Glicksman, Acta Metall. **29**, 701 (1981)
63. R. Trivedi, in *Principles of Solidification and Materials Processing*, vol. 1, ed. by R. Trivedi, J.A. Sekhar, J. Mazumdar (Trans Tech, Aedermannsdorf, 1990), p. 33
64. M.E. Glicksman, J. Cryst. Growth **274**, 317 (2005)
65. H. Kaya, E. Çadırlı, M. Gündüz, Appl. Phys. A **94**, 155 (2009)
66. M.B. Koss, J.C. LaCombe, L.A. Tennenhouse, M.E. Glicksman, E.A. Winsa, Metall. Mater. Trans. A **30**, 3177 (1999)
67. M. Georgelin, A. Pocheau, J. Cryst. Growth **268**, 272 (2004)
68. P. Villars, A. Prince, H. Okamoto, *Handbook of Ternary Phase Diagrams*, vol. 3 (ASM International, Materials Park, 1995), p. 3256
69. J. Lipton, M.E. Glicksman, W. Kurz, Metall. Trans A **18**, 341 (1987)
70. R. Trivedi, W. Kurz, Metall. Trans A **21**, 1311 (1987)
71. M. Gündüz, J.D. Hunt, Acta Metall. **37**, 1839 (1989)
72. Q. Du, D.G. Eskin, L. Katgerman, Metall. Mater. Trans. A **32**, 180 (2007)
73. F.Y. Xie, T. Kraft, Y. Zuo, C.H. Moon, Y.A. Chang, Acta Mater. **47**, 489 (1999)